JOURNAL OF GEOPHYSICAL RESEARCH, VOL. 102, NO. A7, PAGES 14,467-14,476, JULY 1, 1997

Mapping of the ionospheric field-aligned currents to the equatorial magnetosphere

G. Lu,[1] G. L. Siscoe,[2] A. D. Richmond,[1] T. I. Pulkkinen,[3,4] N. A. Tsyganenko,[5] H. J. Singer,[6] and B. A. Emery[1]

Abstract. The assimilative mapping of ionospheric electrodynamics (AMIE)–derived ionospheric field-aligned current patterns during the ninth Coordinated Data Analysis Workshop substorm event have been mapped to the magnetospheric equatorial plane, using the data-based magnetospheric magnetic field model [*Tsyganenko*, 1995]. We find that at the onset of the substorm expansion phase, a pair of field-aligned currents emerges about 8 R_E tailward of the Earth, near the x axis. This pair of field-aligned currents is consistent with the substorm current wedge model; it lines up in the east-west direction across the near-Earth tail current and has the sense of the nightside region 1 current, i.e., flowing into the ionosphere on the east side and out of the ionosphere on the west side. The ionospheric counterpart of the substorm wedge currents in the midnight sector, on the other hand, has a northeast-to-southwest alignment. During the expansion phase, the substorm wedge currents intensify and expand in spatial size; however, their peaks remain nearly at the same location in the equatorial magnetosphere, about 8 R_E tailward from the Earth. We also find that the intensification of the substorm wedge currents during the expansion phase is accompanied by the intensification of the region 2–sense currents located closer to the Earth, and the boundary between the region 2 and substorm wedge currents lies around x = -6 R_E.

Introduction

Despite nearly three decades of extensive studies, substorms are still one of the most interesting and yet often controversial phenomena in magnetospheric physics. Magnetospheric substorms are the manifestation of solar wind/magnetosphere energy release either through the directly driven or the unloading processes or both [e.g., *Akasofu*, 1981]. In the ionosphere, the energy dissipation associated with substorms is the intensification of auroral precipitation and Joule heating. Electric currents play an important role in the energy coupling between the magnetosphere and ionosphere. A classical picture of the substorm current system consists of a pair of field-aligned currents that flow into the ionosphere at the eastward portion of the tail current and flow out of the ionosphere at the westward portion as a result of the disruption or collapse of the cross-tail current, forming the so-called substorm current wedge [*McPherron et al.*, 1973]. The field-aligned currents are closed in the ionosphere through the westward electrojet. One of the key elements in substorm studies is to determine the substorm current system. Though substorm-associated field-aligned currents have been inferred from localized observations at geosynchronous altitude [e.g., *Nagai*, 1982, 1987; *Nagai et al.*, 1987; *Ohtani et al.*, 1990] and from ground-based magnetometer measurements [*Lester et al.*, 1983; *Singer et al.*, 1984; *Hughes and Singer*, 1985], the spatial configuration as well as temporal variation of the substorm current wedge in the magnetosphere is yet to be established.

It is almost impossible to have sufficient simultaneous satellite observations that could physically cover the huge magnetospheric domain involved in a substorm. The low-altitude ionospheric electrodynamic fields, on the other hand, can be relatively well monitored by polar-orbiting satellites and by multiple ground-based instruments. Therefore mapping of the ionospheric fields and currents offers an alternative way to understand the complicated substorm processes in the mag-

[1] High Altitude Observatory, National Center for Atmospheric Research, Boulder, Colorado.

[2] Center for Space Physics, Boston University, Boston, Massachusetts.

[3] On leave from Laboratory for Atmospheric and Space Physics, University of Colorado, Boulder.

[4] Department of Geophysics, Finnish Meteorological Institute, Helsinki.

[5] Hughes STX Corporation, NASA Goddard Space Flight Center, Greenbelt, Maryland.

[6] Space Environment Center, National Oceanic and Atmospheric Administration, Boulder, Colorado.

Paper number 97JA00744.
0148-0227/97/97JA-00744$09.00

netosphere. Indeed, auroral images taken during substorms have been mapped to the equatorial magnetosphere to study their magnetospheric plasma origins by using a magnetic field model [e.g., *Elphinstone et al.*, 1991, 1993; *Pulkkinen et al.*, 1995]. The purpose of this paper is to shed some light on the evolution of the substorm current systems by mapping the ionospheric field-aligned currents to the equatorial magnetosphere.

Data and Model Comparison

When using empirical magnetic field models to study particular events, we implicitly assume that the instantaneous magnetic field line configurations for a specific period can be replicated with a sufficient accuracy, in spite of the fact that the model parameters were derived from observations of different periods under widely different external conditions and with different individual histories of temporal evolution. In this regard, it is important that models have sufficient number of degrees of freedom in their input parameters, allowing for an adequate representation of dynamical effects of the most significant external factors, such as the solar wind pressure and the interplanetary magnetic field (IMF). The accuracy of the model output can also be improved by including additional input parameters that reflect the current state of the main magnetospheric electric current systems. For example, the *Dst* index (after a proper correction for the effect of the magnetopause currents [e.g., *Akasofu*, 1981]) can serve as a parameter controlling the amplitude of the ring current.

In the past, the 1987 and 1989 versions of the data-based magnetic field model [e.g., *Tsyganenko*, 1987, 1989] (hereinafter referred to as T87 and T89, respectively) were often used for mapping ionospheric phenomena. However, those models were parameterized only by the *Kp* index and did not include large-scale effects of the solar wind conditions upon the geomagnetic field configuration.

The drawbacks of the T87/T89 models are largely eliminated in the newly developed models [e.g., *Tsyganenko*, 1995, 1996] (hereinafter referred to as T95 and T96, respectively). The primary features of the T95 and T96 models include an explicitly defined realistic magnetopause whose size is determined by the solar wind pressure, the IMF-controlled penetration of the solar wind magnetic field inside the magnetosphere, and a separate representation for the field of Birkeland current systems. The ring current in the new models is parameterized by the *Dst* index. The T96 model differs from T95 mainly in three aspects. First, shorter expansions are used to represent the shielding fields for all sources of the external field and a simpler representation for the tail and ring current terms is employed, which results in much faster performance of the model codes. Second, a more realistic model for the region 2 Birkeland current system is devised, with a more spread-out radial distribution of the partial ring current density, which avoids

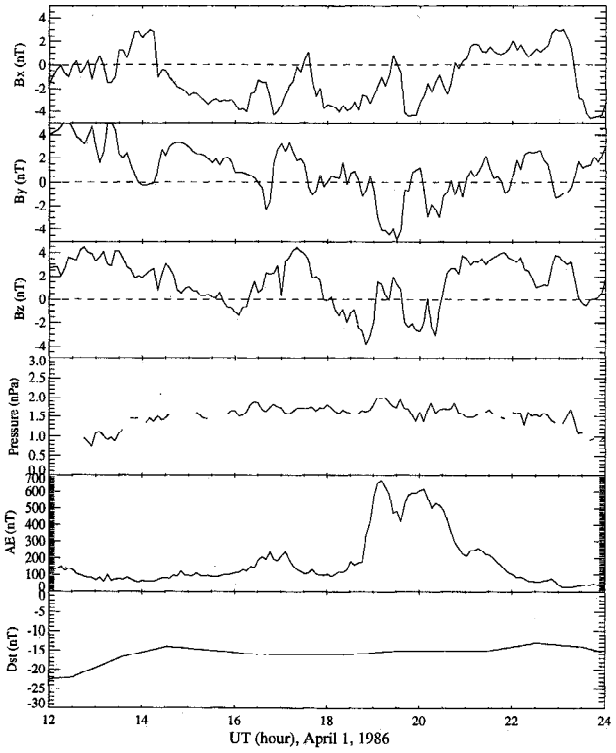

Figure 1. (top to bottom) Interplanetary magnetic field (IMF) B_x, B_y, and B_z components in GSM coordinates, the solar wind dynamic pressure, *AE*, and *Dst* between 1200 and 2400 UT on April 1, 1986.

the unphysical kink on the nightside radial profile of the B_z component in the T95 model. Third, since the *AE* index, which is one of the input parameters in the T95 version to specify the region 2 current density, has a small regression coefficient with the model field; the latest T96 version is independent of *AE*.

Figure 1 shows the IMF and solar wind parameters measured by IMP 8 between 1200 and 2400 UT on April 1, 1986. IMP 8 was located at about (29,22,11) R_E in GSE coordinates at 1900 UT. During the interval, all three components of the IMF oscillated in sign, with a magnitude less than 5 nT. IMF B_z was primarily northward before 1800 UT and turned southward about 50 min prior to the substorm. Also shown in Figure 1 is the *AE* index. Unlike the standard *AE* index, which is based on the ground magnetic perturbations in the north-south component from 12 selected auroral zone stations, the *AE* index plotted in Figure 1 is derived from 53 stations located between 55° and 76° magnetic latitude. Figure 1 (bottom) is the standard 1-hour *Dst* index. The stable and small magnitude of *Dst* indicates that there were no magnetic storms during the period.

The solar wind dynamic pressure, IMF B_y and B_z, *Dst* and *AE* are the five input parameters for the T95 model; for T96, the first four parameters are the inputs. The T89 model is driven by the *Kp* index only.

For this study, the region of most interest is the inner part of the nightside equatorial magnetosphere (within 10 R_E of the Earth). In order to find out which

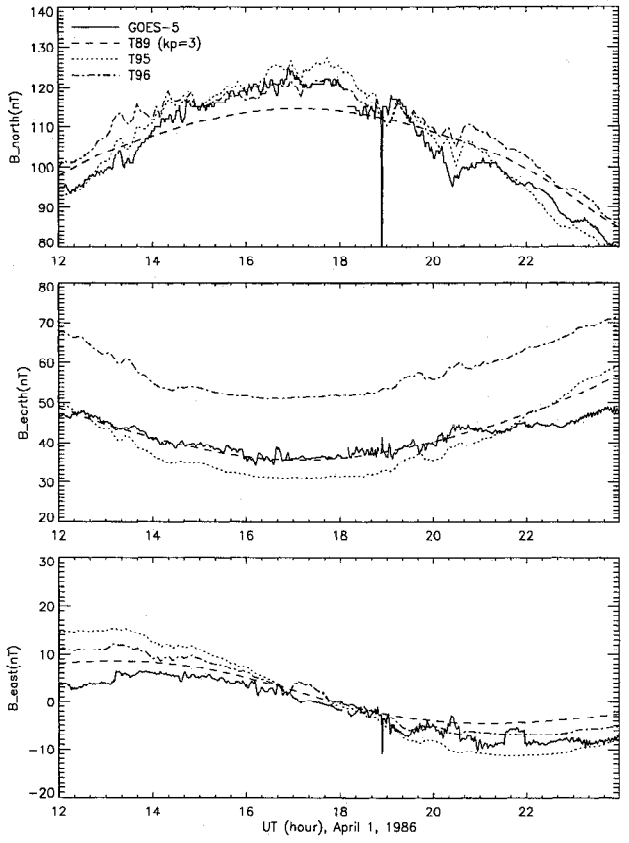

Figure 2. Comparison between the GOES 5 measurements and the different magnetic field models, *Tsyganenko* [1989, 1995, 1996] (T89, T95, T96).

model is most suitable for this event, we have compared the magnetic field components measured by geosynchronous satellites during the 12-hour period with those provided by the different models. Figures 2 and 3 show comparisons of the 1-min magnetic fields measured by GOES 5 and GOES 6 with the T89, T95, and T96 models, respectively. The GOES 5 and GOES 6 satellites were located at geosynchronous orbit; at 1900 UT, when the substorm occurred, GOES 5 was located at about 1400 MLT and GOES 6 at about 1200 MLT. All three model runs use the dipole internal magnetic field, with a tilt angle calculated from the instantaneous direction of the Sun at each time step. Using the International Geomagnetic Reference Field (IGRF) as the internal field results in an insignificant change in the calculated components (less than 3 nT).

Plotted in Figure 2, from top to bottom, are the northward (parallel to geographic north), earthward, and eastward components. The solid line is the satellite measurement, the dashed line is the T89 model field for Kp=3 which was the value corresponding to the event, the dotted line is the T95 model with current time *Dst* and *AE* and a 10-min delay for the solar wind parameters to account for the propagation time, and the dash-dotted line is the T96 model results. The T95 model results show very good agreement with the field measured by GOES 5, even the smaller-scale variations. The T89 model agrees with the GOES 5 observations in terms of their general large-scale variations but is unable to reproduce the small-scale features. T96 also shows generally good agreement with the GOES 5 measurements in both northward and eastward components, but the earthward component from T96 is about 15 nT larger than the observations. Similarly, as shown in Figure 3, the agreement between T95 and the GOES 6 measurements is reasonably good for the earthward and eastward components. Again, T89 shows general agreement with the GOES 6 observations, but it does not do as well as the T95 model in terms of small-scale features. The T96 model has better agreement than T95 with the GOES 6 eastward component, but again, its earthward component is about 15 nT larger than the observations. The large discrepancy in the T96 earthward (or radial) component should be attributed to an inaccuracy in the characteristic thickness of the model ring current. As mentioned above, the T96 model employs a simplified representation for the ring current field, in which the scale size of the distribution of the electric current density in the north-south direction does not depend on the local time. As a result, the model ring current is probably too thin on the dayside, which leads to an overestimate of the radial field component. It should also be noted that in the existing data sets on which T96 is based, the data points are insufficient in the low-latitude inner magnetosphere to allow a reliable deter-

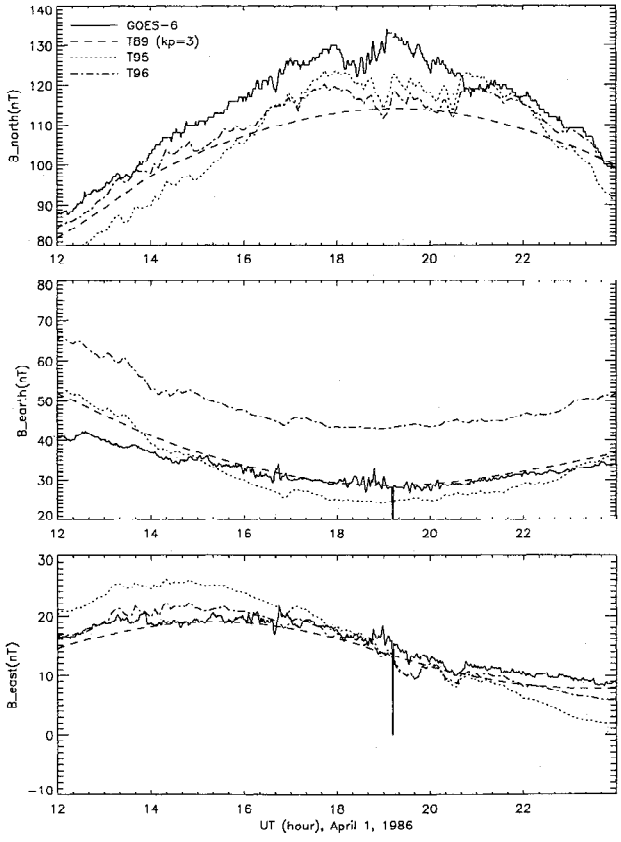

Figure 3. Comparison between the GOES 6 measurements and the different magnetic field models.

mination of the structure of the ring current and of the region 2 system of Birkeland currents. Therefore, until more data (e.g., CRRES, Active Magnetospheric Particle Tracer Explorers (AMPTE)CCE, and GOES) are added to the existing database, it is unlikely that significant improvement of models' performance will occur in the geosynchronous region.

Although there is a similar trend exhibited by the northward component both in the models and in the GOES 6 measurements, the magnitude of T95 is about 10 to 15 nT smaller than the observation, and T89 and T96 are 5 to 20 nT smaller than the observation. Some of these differences may be due to the difficulty of measuring the magnetic field with the spin axis (in this case, northward) sensor on a spinning spacecraft. It is not possible to routinely determine a good magnetometer sensor offset along the spin axis and changes that occur in both the instrument electronics and spacecraft environment can affect these measurements during the satellite lifetime. Some of these difficulties are discussed by *Fairfield and Zanetti* [1989] and *Lopez and von Rosenvinge* [1993] in their use of the GOES magnetometer data. By comparing the GOES measurements with the AMPTE/CCE data, they found, on average, the GOES northward component is offset 5 to 10 nT from the CCE measurements, and the offset appears to vary with time [*Lopez and van Rosenvinge*, 1993]. We therefore attribute the difference in the northward component between GOES 6 and T95 to the magnetometer baseline offset. Unfortunately, there were no CCE data available to verify this.

Figures 2 and 3 show that all three magnetic field models generally agree with the GOES observations on the dayside; however, the T89 model is unable to reproduce the smaller-scale variations, and T96 tends to have a larger earthward component than the observations. We therefore choose T95 to map the ionospheric field-aligned current into the magnetospheric equatorial plane in the study. We should point out that because there are no satellite magnetic field observations available on the nightside during the period under study, we are unable to test how realistically the T95 model represents the magnetotail configuration. However, we do not expect significant alteration in the features that are mapped to the equatorial plane within 10 R_E of the Earth. We will discuss this in more detail in the Summary and Discussion section.

Field-Aligned Current Mapping

In this section, we map the ionospheric field-aligned current patterns to the equatorial magnetosphere, using the T95 model. The purpose of doing so is to understand how the substorm current wedge evolves in the equatorial plane.

The event reported here is one of the ninth Coordinated Data Analysis Workshop (CDAW 9) substorm intervals. The onset of the substorm expansion phase occurred at 1850 UT on April 1, 1986, as manifested by the sudden brightening of aurora observed by the Viking satellite, along with the simultaneous sharp increase of the *AE* index shown in Figure 1. The peak of the expansion phase occurred at 1905 UT; after that, the substorm was in the recovery phase as *AE* gradually decreased. However, before the ionosphere fully recovered, another substorm started at about 1940 UT. We focus on the interval between 1840 and 1905 UT. This was a moderate substorm, with *AE* less than 700 nT. *Dst* was nearly steady, about -15 nT.

The assimilative mapping of ionospheric electrodynamics (AMIE) procedure is an optimally constrained, weighted, least squares fit of coefficients to the observations [*Richmond and Kamide*, 1988]. It first estimates the height-integrated Pedersen and Hall conductances by modifying statistical conductance models with various direct and indirect observations. In this study, the initial statistical conductance model is the precipitating electron model (PEM) of *Kroehl et al.* [1988], which is based on the DMSP precipitating electron data and is parameterized to 10 levels (from 0 to 9) of activity index according to the equatorward auroral boundary at midnight. An example of the initial Pedersen and Hall conductances at 1905 UT is shown in Figures 4a and 4c, corresponding to the activity index of 5. Both Pedersen and Hall conductances are enhanced within the auroral zones.

The Viking UV images provide valuable information regarding the ionospheric conductivity [*Lummerzheim et al.*, 1991; *Rees et al.*, 1995; H. W. Kroehl, private communication, 1993]. To derive the conductances, the Viking UV luminosity data are first averaged over bins 1° in latitude and 1 hour in magnetic local time (MLT). The height-integrated Pedersen conductances are then calculated for each bin, using the algorithm of *Robinson et al.* [1989] (see also *Ahn et al.* [1995] for more details). In deriving the Hall conductance [*Robinson et al.*, 1989], the average energies from the PEM model at the corresponding activity level are used. In addition to the Viking UV images, the magnetic perturbations measured by ground magnetometers are also used to modify the conductivity [*Ahn et al.*, 1983]. During the period under study, the European Incoherent Scatter (EISCAT) radar was operating in the CP-3-E mode [*Winser et al.*, 1989], which provided both height-integrated ionospheric conductances and ion drift vectors. At 1905 UT, Pedersen and Hall conductances measured by EISCAT at 68.7° magnetic latitude and 21.4 MLT are 9.31 and 19.47 S, respectively. The EISCAT measurements are consistent with the conductances inferred from the Viking image at the same location. The fitted Pedersen and Hall conductances are shown in Figures 4b and 4d, which are obtained by modifying the PEM model with direct conductance observations by the EISCAT radar and indirect measurements of the conductances from both Viking images and ground magnetometer data as described by *Richmond et al.* [1988]. The enhancement

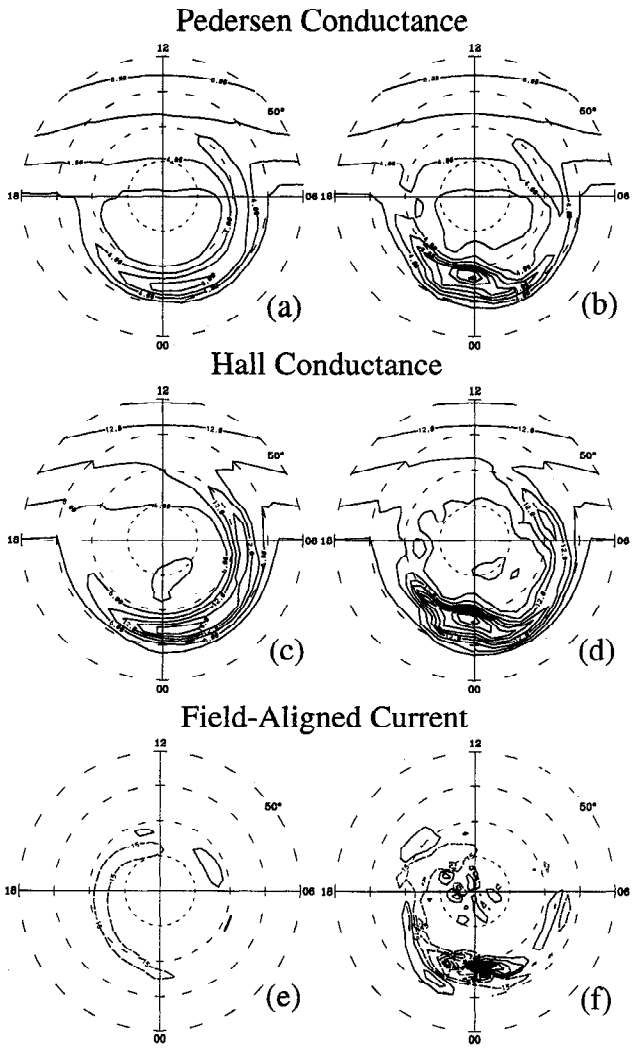

Figure 4. Distributions of Pedersen (a) model and (b) fitted pattern and Hall (c) model and (d) fitted pattern conductances as well as (e) model and (f) fitted pattern field-aligned currents at 1905 UT. The contour interval is 2 S for the Pedersen conductance, 3 S for the Hall conductance, and 0.3 μA/m^2 for field-aligned current.

of ionospheric conductances in the midnight sector is due to the intensification of auroral luminosity observed by Viking.

Once the conductivity distribution is estimated, the ionospheric electric potential or convection pattern can be estimated from the direct observations from satellites and radars and from the inversion of ground magnetic field measurements. During the CDAW 9 event, the EISCAT and Millstone Hill incoherent scatter radars as well as the Sweden and Britain Radar-Auroral Experiment (SABRE) coherent scatter radar were operating, along with 90 ground magnetometers. The good data coverage allows AMIE to achieve relatively satisfactory estimates of the ionospheric conductance and electric field. Field-aligned currents are then derived from the divergence of the ionospheric horizontal current, which depends on both the electric field and the conductivity. Figure 4f shows the distribution of field-aligned current at 1905 UT, with the most intense field-aligned currents in the midnight sector. As a comparison, Figure 4e show the field-aligned current pattern derived from the initial statistical conductances shown in Figures 4a and 4c, along with the statistical electric potential model of *Foster et al.* [1986] (not shown). As one can see, the field-aligned currents derived from the model inputs totally miss the intensification in the midnight sector associated with the substorm, which is the main feature that will be examined in this paper.

Figure 5 shows the 5-min patterns of field-aligned current in the northern hemisphere during the substorm growth and expansion phases between 1840 and 1905 UT, derived from AMIE. We do not consider the recovery phase in this study; because of the lack of Viking auroral images, we are not so confident about the ionospheric conductivities after 1910 UT. The solid contours represent downward currents, and the dashed contours represent upward currents. The contour interval is 0.3 μA/m^2, starting at $\pm$0.15 μA/m^2. At 1840 and 1845 UT, the large-scale distribution shows upward region 1 and downward region 2 currents on the duskside and downward region 1 current on the dawnside, but the upward region 2 current on the dawnside is too weak to appear at the 0.3 μA/m^2 contour level. Note that because of the relatively small IMF magnitude, the field-aligned current is rather weak and the total hemisphere-integrated downward current given at the upper right is only around 1 MA. At 1850 UT, the onset of the substorm expansion phase, the currents at dawn and dusk remain the same, but a pair of field-aligned currents emerges in the local midnight region, with the downward current located northeastward of the upward current. This pair of field-aligned currents is often referred to as the substorm current wedge [*McPherron et al.*, 1973]. As the substorm progresses, the wedge currents become more intense. We would like to mention that the distribution of the upward field-aligned current in the midnight sector agrees quite well with the location of intense auroral emission shown in the Viking images, which give us confidence in the field-aligned current patterns derived from AMIE. The northeast-to-southwest distribution of field-aligned currents shown in Figure 5 also resembles the ionospheric current model of *Samson* [1985].

We then use the T95 model to map the ionospheric field-aligned currents to the equatorial magnetosphere. In so doing, we artificially assume that there is no current leakage across the magnetic field lines between the polar ionosphere and the equatorial magnetosphere so that the projection of ionospheric field-aligned current density at the equatorial plane is scaled as

$$j_e = \frac{B_e}{B_i} j_i \tag{1}$$

where the subscripts i and e denote to the ionosphere and equator, respectively. Instead of the common minimum $|B|$ plane, the equator is defined as the locus of

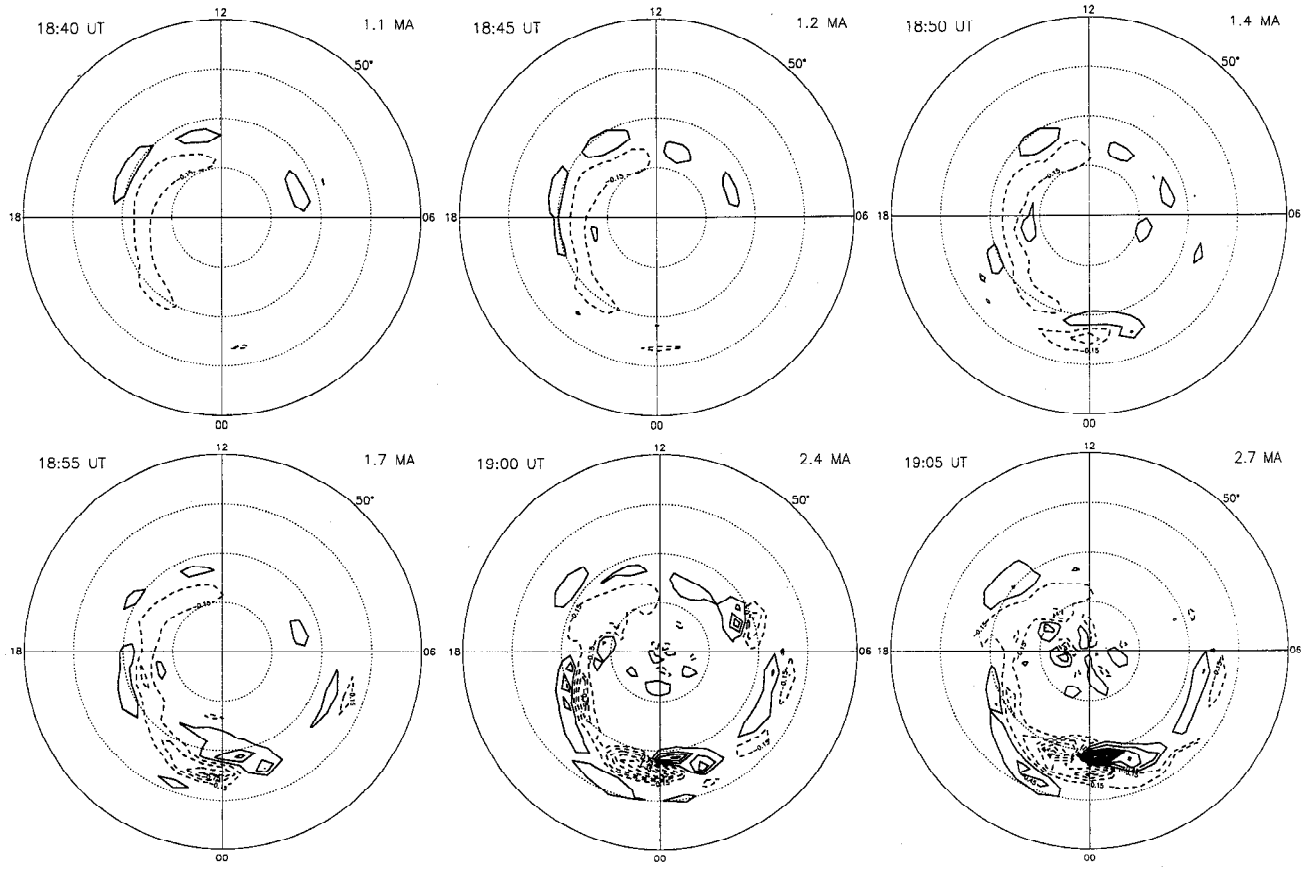

Figure 5. The 5-min patterns of field-aligned current density in the northern hemisphere between 1840 and 1905 UT on April 1, 1986. The solid contours represent downward currents, and the dashed contours are for upward currents. The contour interval is 0.3 μA/m^2, starting at $\pm$0.15 μA/m^2. The total downward field-aligned current integrated poleward of 50° is given at top right.

the farthest points away from the Earth along the closed magnetic field lines. This is to avoid difficulty near the cusp regions, where the minimum $|B|$ is often located in the high-latitude magnetopause. Figure 6 shows the projection of the magnetic field lines along the noon-midnight meridian in the x-z plane in GSM coordinates.

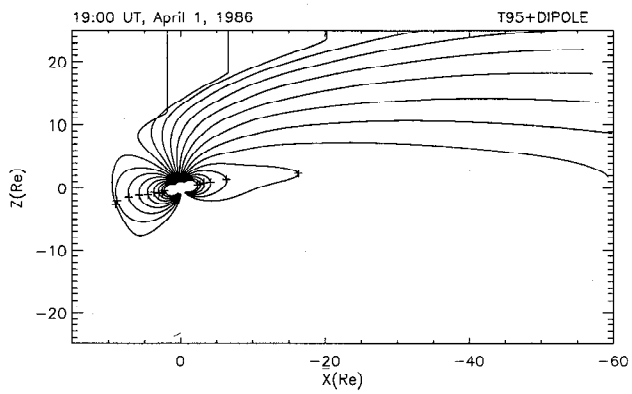

Figure 6. Field line projection to the x-z plane in GSM coordinates. The plus signs indicate the equator as defined by the most distant point of the closed field line from the Earth.

The plus signs indicate the equator. We should point out that j_e would be the true equatorial field-aligned current density only if the diversion of perpendicular currents was within a thin layer located near the equator. In reality, however, the layer of perpendicular current is a few Earth radii thick [e.g., *Birn and Hesse*, 1996]. What j_e actually represents, then, is a measure of the divergence of perpendicular current, integrated through the thickness of this layer.

Figure 7 shows the mapped field-aligned current in the equatorial plane. The solid (dashed) contours indicate currents that flow out of (into) the equatorial plane, with a contour interval of 0.3 nA/m^2. The time sequence goes from left to right and from top to bottom. The nonsubstorm-associated region 1 current maps to the equatorial plane along the magnetopause on both the dawnside and duskside, and the region 2 current maps farther earthward of the magnetopause on the duskside. One of the interesting features of these equatorial current maps is the appearance of a pair of region 2–sense field-aligned currents on the nightside. The region 2 currents do not exactly show up in the corresponding ionospheric maps for the given contour interval; they show up in the equatorial maps because

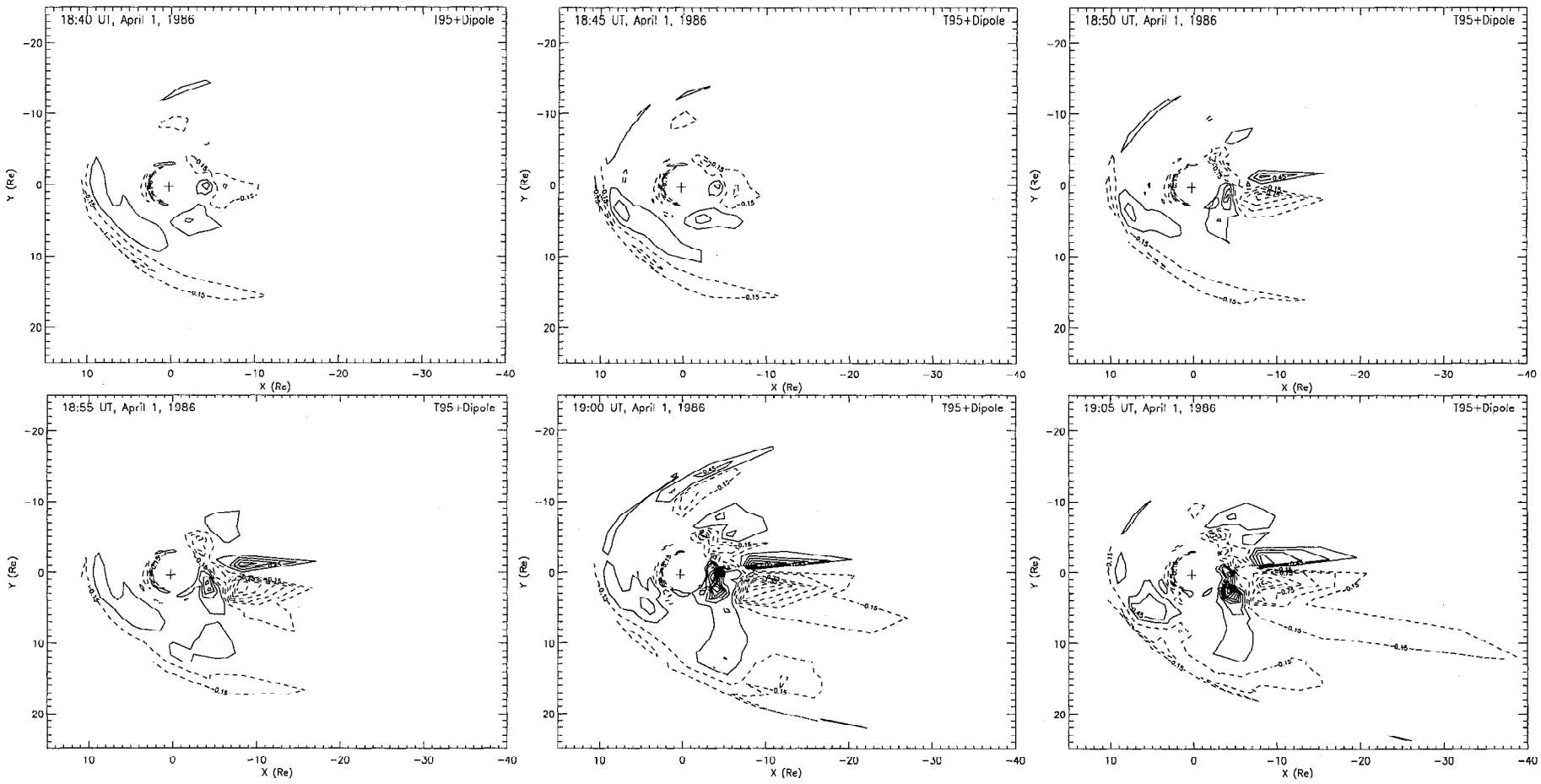

Figure 7. Mapping of field-aligned current in the equatorial plane. The solid (dashed) contours indicate the currents that flow out of (into) the equatorial plane, with a contour interval of 0.3 nA/m2.

the contour interval is 3 orders smaller than that for the ionospheric maps. Note also that the mapping factor B_e/B_i becomes relatively larger when closer to the Earth so that the lower-latitude features tend to be more enhanced than the high-latitude ones when being mapped to the equatorial plane. Before the substorm onset, these region 2–sense currents are centered 6 R_E away from the Earth. Additionally, some smaller-scale currents also appear sunward of the Earth, at about 3 R_E. At 1850 UT, the onset of the substorm expansion phase, another pair of field-aligned currents that flow in the opposite direction to the region 2–sense currents emerges near the x axis, with peaks around 8 R_E tailward of the Earth. This substorm current wedge system appears to push the region 2–sense currents toward the Earth, from 6 to 4 R_E. During the expansion phase between 1850 and 1905 UT, the substorm current wedge not only intensifies in magnitude, but also expands in spatial size; however, the current peaks remain at the same location at about x = -8 R_E. At the same time, the region 2–sense currents are also enhanced.

It is noteworthy that the substorm wedge currents line up not only in the east-west direction, but also in the north-south direction in the ionosphere; their equatorial projection, on the other hand, is nearly in the east-west direction. This is because in the stretched magnetic field configuration, the mapping factor becomes smaller as one moves farther away from the Earth, which thus emphasizes only the near-Earth portion of the current system. For instance, at 1900 UT, the tailward tip of the equatorial wedge current that flows into the ionosphere (shown as solid contours in Figure 7) at about x = -20 R_E has its ionospheric foot point at 67° magnetic latitude near midnight. By examining the corresponding ionospheric field-aligned current pattern at 1900 UT in Figure 5, one can see that about 30% of the substorm-associated field-aligned current in the midnight sector is located above 67°. This portion of the current maps to a large region in the distant tail beyond 20 R_E from the Earth, where the current density is very low because of the diverging magnetic field topology.

The higher-latitude field lines are often stretched so that they may not cross the equatorial plane until reaching the distant tail. Unlike the direct field line mapping of auroral images, in which the discrete aurora often maps to 30 R_E or beyond, suggesting a magnetospheric plasma source in the plasma sheet boundary layer [*Elphinstone et al.*, 1993; *Pulkkinen et al.*, 1995], the mapping of field-aligned currents has to take into account the mapping factor. As a result, the main magnetospheric effects of the current wedge (caused by the most intense current density) are located close to the Earth, near the geosynchronous orbit. An interesting effect of the mapping factor is that although the Viking images have shown poleward motion of the auroral oval during the substorm expansion phase (and so do the nightside upward field-aligned currents in the AMIE patterns), the equatorial mapping of the substorm wedge currents shows no corresponding tailward motion and the peaks of the wedge currents remain nearly steady at about x = -8 R_E.

During the substorm expansion phase, the ionospheric maps in Figure 5 show clearly the intensification of the substorm wedge current in the east-west direction. The corresponding equatorial maps in Figure 7 also show the similar expansion in the Y direction but not as dramatically as in the ionosphere. This is partially due to the fact that as the wedge current expands in the east-west dimension, the center of the current also moves poleward. For instance, at 1850 UT, the center of the upward wedge current in the ionosphere was at about 65° magnetic latitude; but at 1900 UT, it had moved to about 67°. The northeast-to-southwest alignment of the ionospheric substorm wedge currents is also the cause of asymmetry in the equatorial current maps in which the density of the currents that flow into the ionosphere (Figure 7, solid contours) is weaker than the currents that flow out of the ionosphere (Figure 7, dashed contours).

Summary and Discussion

By testing the different versions of the magnetic field models against the GOES observations, T95 appears to be the one that represents more realistically, relatively speaking, the dayside large-scale magnetosphere during this particular event. The mapping of ionospheric field-aligned current to the equatorial plane using T95 has revealed some interesting characteristics of the substorm wedge currents: (1) they emerge at the onset of the substorm expansion phase with an east-west alignment, even though their ionospheric counterpart lines up in the northwest-to-southeast direction; (2) they not only intensify in magnitude, but also expand in spatial distribution during the expansion phase, however, the peaks of the wedge currents remain nearly steady at about x = -8 R_E; and (3) the intensification of the substorm current wedge is accompanied by the intensification of the region 2–sense currents located further earthward, and the boundary between the substorm wedge currents and the region 2 currents is around x = -6 R_E. As a comparison, we have also used the T96 model to map the ionospheric field-aligned current. We find that the difference between the T96 mapping and T95 mapping is minimal (mainly in some small-scale structures), and all three characteristics associated with the substorm current system, as stated above, remain the same.

Our equatorial mapping of field-aligned currents shown in Figure 7 is consistent with the field-aligned current signatures inferred from the geosynchronous satellite observations reported by *Nagai* [1982, 1987] and *Ohtani et al.* [1990], who found that the substorm-associated region 1 currents are not just the enhancement of the preexisting current system in the near-Earth region; they arise as a result of cross-tail current

disruption. *Ohtani et al.* [1990] also pointed out the importance of the region 2 currents, which form inside of the geosynchronous orbit during substorm, as part of the substorm current system. They proposed that the radial current component that connects the region 2 and substorm-associated region 1 currents acts as a magnetospheric dynamo that converts mechanical energy into electromagnetic energy. If so, our study shows that this dynamo region is around 6 R_E tailward of the Earth.

A recent MHD simulation by *Birn and Hesse* [1996] reveals that the field-aligned current generation takes place well earthward of the reconnection site as a result of the diversion of perpendicular currents. Their simulation shows that a field-aligned current of region 1 type, generated mainly in the velocity shear layer 1 R_E above the equatorial plane, occupies the region from x = -5 to -13 R_E. Our results agree with the MHD simulation, though the distribution of our mapped field-aligned current in the equatorial plane covers a relatively wider and yet more tailward range from x = -6 to about -20 R_E. This is partially due to the fact that the current distribution from the MHD simulation is 1 R_E above the equator, whereas we have mapped the field-aligned current into the equatorial plane. Because of the stretched tail field lines, the field-aligned current projection would become more tailward in the equatorial plane than in the plane above the equator.

We should emphasize that the accuracy of the field line mapping depends on the accuracy of the magnetic field model that has been applied. Though the magnetic field models are based on statistical studies, we find that they agree reasonably well with the GOES satellite observations in the dayside magnetosphere. Because the T95 model incorporates time-varying input parameters (e.g., solar wind pressure, IMF, *AE*, *Dst*) to specify the main magnetospheric current systems, including the region 1 and region 2 currents, the ring current, and the cross-tail current, it can even reproduce some smaller-scale variations. The good agreement of the temporal evolution between the model and observation also reflects the fact that the dayside magnetic field variations are directly driven by variations in the solar wind and IMF parameters.

On the other hand, the nightside magnetosphere includes two types of field variations, those driven directly by solar wind variations and those related to episodes of energy loading and unloading during substorms. During the loading-unloading activity, the field configuration depends not only on the present values of solar wind and IMF parameters, but also on their time history. Therefore the statistical picture is not as well representative of the field configuration during these times. The lack of satellite observations in the nightside tail during the substorm prevents us from assessing the details of the magnetic mapping shown in Figure 7. Previous case studies [e.g., *Pulkkinen et al.*, 1991] suggest that the tail field becomes more dipolarized at the onset of the substorm expansion phase and retains a dipolarized shape throughout the expansion phase. Owing to the lack of in situ measurements, we have chosen to show the mappings using the T95 model with the appropriate input parameters. We estimate that the field dipolarization would have largest effects in the distant tail (beyond 10 R_E from the Earth) that is outside the current maximum region and thus are confident that the main conclusion about the location of the current maximum is not affected by the choice of the field model. However, in the dipolarized field configuration, the outer contours now stretching out to tens of Earth radii would map much closer to the current maximum region.

The field-aligned currents themselves also produce a perturbation to the ambient magnetic field and thus change the mapping [e.g., *Pulkkinen et al.*, 1990; *Donovan*, 1993]. However, the effect of a pair of wedge-like currents is to shift the mappings farther tailward; effects in the east-west direction are small.

Because the field inward of the geosynchronous orbit does not change very much during substorm activity and because there should not be significant sources for mapping errors in the Y direction, we are relatively confident that our mapping of ionospheric field-aligned currents to the magnetospheric equatorial plane offers a reasonably representative overview of the evolution of the substorm current system. Furthermore, the mapping of field-aligned current also provides a context for the interpretation of geosynchronous satellite observations.

Acknowledgments. We would like to thank M. Hesse for helpful discussion. The work at HAO/NCAR was supported in part by the NSF grant 93-SFA.1 and by the NASA Space Physics Theory Program and NASA grant W-18,536. The work at Boston University was supported by NSF under grant ATM95-03423. The work of T. P. was funded by the Finnish Fulbright Commission.

The Editor thanks E. Nielsen and K. B. Baker for their assistance in evaluating this paper.

References

Ahn, B.-H., R. M. Robinson, Y. Kamide, and S.-I. Akasofu, Electric conductivities, electric fields and auroral energy injection rate in the auroral ionosphere and their empirical relations to the horizontal magnetic disturbances, *Planet. Space Sci., 31*, 641, 1983.

Ahn, B.-H., Y. Kamide, H. W. Kroehl, M. Candidi, and J. S. Murphree, Substorm changes of the electrodynamic quantities in the polar ionosphere: CDAW 9, *J. Geophys. Res., 100*, 23,845, 1995.

Akasofu, S.-I., Energy coupling between the solar wind and the magnetosphere, *Space Sci. Rev., 28*, 121, 1981.

Birn, J., and M. Hesse, Details of current disruption and diversion in simulations of magnetotail dynamics, *J. Geophys. Res., 101*, 15,345, 1996.

Donovan, E. F., Modeling the magnetic effects of field-aligned currents, *J. Geophys. Res., 98*, 13,529, 1993.

Elphinstone, R. D., D. Hearn, J. S. Murphree, and L. L. Cogger, Mapping using the Tsyganenko long magnetospheric model and its relationship to Viking auroral images, *J. Geophys. Res., 96*, 1467, 1991.

Elphinstone, R. D., J. S. Murphree, D. J. Hearn, W. Heikkila, M. G. Henderson, L. L. Cogger, and I. Sandahl, The auroral distribution and its mapping according to substorm phase, *J. Atmos. Terr. Phys., 55*, 1741, 1993.

Fairfield, D. H., and L. J. Zanetti, Three-point magnetic field observations of substorms in the inner magnetosphere, *J. Geophys. Res., 94*, 3565, 1989.

Foster, J. C., J. M. Holt, R. G. Musgrove, and D. S. Evans, Ionospheric convection associated with discrete levels of particle precipitation, *Geophys. Res. Lett., 13*, 656, 1986.

Hughes, W. J., and H. J. Singer, Midlatitude Pi 2 pulsations, geosynchronous substorm onset signatures and auroral zone currents on March 22, 1979: CDAW-6, *J. Geophys. Res., 90*, 1297, 1985.

Kroehl, H. W., J. F. McKee, K. R. Lutz, D. J. Gorney, and C.-I. Meng, A realistic model of high-latitude conductance produced by precipitating electrons, *Eos Trans. AGU, 69* (44), 1356, 1988.

Lester, M., W. J. Hughes, and H. J. Singer, Polarization patterns of Pi 2 magnetic pulsations and the substorm current wedge, *J. Geophys. Res., 88*, 7958, 1983.

Lopez, R. E., and T. von Rosenvinge, A statistical relationship between the geosynchronous magnetic field and substorm electrojet magnitude, *J. Geophys. Res., 98*, 3851, 1993.

Lummerzheim, D., M. H. Rees, J. D. Craven, and L. A. Frank, Ionospheric conductances derived from DE-1 auroral images, *Planet. Space Sci., 53*, 281, 1991.

McPherron, R. L., C. T. Russell, and M. P. Aubry, Satellite studies of magnetospheric substorms on August 5, 1968, 9, Phenomenological model for substorms, *J. Geophys. Res., 78*, 3131, 1973.

Nagai, T., Observed magnetic substorm signatures at synchronous altitudes, *J. Geophys. Res., 87*, 4405, 1982.

Nagai, T., Field-aligned currents associated with substorms in the vicinity of synchronous orbit, 2, GOES 2 and GOES 3 observations, *J. Geophys. Res., 92*, 2432, 1987.

Nagai, T., H. J. Singer, B. G. Ledley, and R. C. Olsen, Field-aligned currents associated with substorms in the vicinity of synchronous orbit, 1, The July 5, 1979, substorm observed by SCATHA, GOES 3 and GOES 2, *J. Geophys. Res., 92*, 2425, 1987.

Ohtani, S., S. Kokubun, R. Nakamura, R. C. Elphic, C. T. Russell, and D. N. Baker, Field-aligned current signatures in the near-tail region, 2, Coupling between the region 1 and region 2 system, *J. Geophys. Res., 95*, 18,913, 1990.

Pulkkinen, T. I., H. E. J. Koskinen, and R. J. Pellinen, Inclusion of field-aligned currents in mapping of auroral structures during substorms, *Eos Trans. AGU*, 71, 1555, 1990.

Pulkkinen, T. I., D. N. Baker, D. H. Fairfield, R. J. Pellinen, J. S. Murphree, R. D. Elphinstone, R. L. McPherron, J. F. Lopez, and T. Nagai, Modeling the growth phase of a substorm using the Tsyganenko model and multi-spacecraft observations: CDAW 9, *Geophys. Res. Lett., 18*, 1963, 1991.

Pulkkinen, T. I., D. N. Baker, R. J. Pellinen, J. S. Murphree, and L. A. Frank, Mapping of the auroral oval and individual arcs during substorms, *J. Geophys. Res., 100*, 21,987, 1995.

Rees., M. H., D. Lummerzheim, and R. G. Roble, Model of the atmosphere-magnetosphere-ionosphere system MAMI, *Space Sci. Rev., 71*, 691, 1995.

Richmond, A. D., and Y. Kamide, Mapping electrodynamic features of the high-latitude ionosphere from localized observations: Technique, *J. Geophys. Res., 93*, 5741, 1988.

Richmond, A. D., et al., Mapping electrodynamic features of the high-latitude ionosphere from localized observations: Combined incoherent-scatter radar and magnetometer measurements for January 18-19, 1984, *J. Geophys. Res., 93*, 5760, 1988.

Robinson, R. M., R. R. Vondrak, J. D. Craven, L. A. Frank, and K. Miller, A comparison of ionospheric conductances and auroral luminosities observed simultaneously with Chatanika radar and the DE 1 auroral images, *J. Geophys. Res., 94*, 5382, 1989.

Samson, J. C., Large-scale studies of Pi-2's associated with auroral breakups, *J. Geophys. Res., 56*, 133, 1985.

Singer, H. J., W. J. Hughes, D. J. Knecht, M. Lester, and C. Gelpi, Ground-satellite observations of substorm related Pi 2 pulsations and current systems, in *Proceedings of the Symposium on the 'Achievements of the IMS', Eur. Space Agency Spec. Publ., ESA SP217*, 679, 1984.

Tsyganenko, N. A., Global quantitative models of geomagnetic field in the cislunar magnetosphere for different disturbance levels, *Planet. Space Sci., 35*, 1347, 1987.

Tsyganenko, N. A., A magnetospheric magnetic field model with a warped tail current sheet, *Planet. Space Sci., 37*, 5, 1989.

Tsyganenko, N. A., Modeling the Earth's magnetospheric magnetic field confined within realistic magnetopause, *J. Geophys. Res., 100*, 5599, 1995.

Tsyganenko, N. A., Effects of the solar wind conditions on the global magnetospheric configuration as deduced from data-based field models, in *Proceedings of the ICS-3 Conference, Versailles, France, May 12-17, 1996, ESA SP-389*, pp. 181-185, 1996.

Winser, K. J., M. Lockwood, G. O. L. Jones, and K. Suvanto, Observations of nonthermal plasmas at different aspect angles, *J. Geophys. Res., 94*, 1439, 1989.

B. A. Emery, G. Lu, and A. D. Richmond, High Altitude Observatory, National Center for Atmospheric Research, 3540 Mitchell Lane, Boulder, CO 80301. (e-mail: ganglu@ucar.edu)

T. I. Pulkkinen, Department of Geophysics, Finnish Meteorological Institute, PO Box 503, FIN-00101 Helsinki, Finland. (e-mail: tuija.pulkkinen@fmi.fi)

H. J. Singer, Space Environment Center, National Oceanic and Atmospheric Administration, 325 Broadway, Boulder, CO 80303. (e-mail: hsinger@sec.noaa.gov)

G. L. Siscoe, Center for Space Physics, Boston University, 725 Commonwealth Avenue, Boston, MA 02215. (e-mail: siscoe@buasta.bu.edu)

N. A. Tsyganenko, Hughes STX Corporation, MC 695, NASA Goddard Space Flight Center, Greenbelt, MD 20771. (e-mail: ys2nt@lepvax.gsfc.nasa.gov)

(Received October 14, 1996; revised March 3, 1997; accepted March 4, 1997.)